

# Interstitial fractionalization and spherical crystallography

Mark J. Bowick<sup>1\*</sup> David R. Nelson<sup>2†</sup> and Homin Shin<sup>1‡</sup>

<sup>1</sup>Physics Department, Syracuse University,  
Syracuse, NY 13244-1130, USA

<sup>2</sup>Lyman Laboratory of Physics, Harvard University,  
Cambridge, MA 02138, USA

October 30, 2018

## Abstract

Finding the ground states of identical particles packed on spheres has relevance for stabilizing emulsions and a venerable history in the literature of theoretical physics and mathematics. Theory and experiment have confirmed that defects such as disclinations and dislocations are an intrinsic part of the ground state. Here we discuss the remarkable behavior of vacancies and interstitials in spherical crystals. The strain fields of isolated disclinations forced in by the spherical topology literally rip interstitials and vacancies apart, typically into dislocation fragments that combine with the disclinations to create small grain boundary scars. The fractionation is often into three charge-neutral dislocations, although dislocation pairs can be created as well. We use a powerful, freely available computer program to explore interstitial fractionalization in some detail, for a variety of power law pair potentials. We investigate the dependence on initial conditions and the final state energies, and compare the position dependence of interstitial energies with the predictions of continuum elastic theory on the sphere. The theory predicts that, before fragmentation, interstitials are repelled from 5-fold disclinations and vacancies are attracted. We also use vacancies and interstitials to study low energy states in the vicinity of “magic numbers” that accommodate regular icosahedral tessellations.

---

\*bowick@physics.syr.edu

†nelson@cmt.harvard.edu

‡hshin@physics.syr.edu

# 1 Introduction

Producing stable emulsions of two immiscible fluids, such as oil and water, is a challenging and important problem, not only because of technical applications but also from the perspective of fundamental science. One strategy for stabilizing emulsions, dating back at least 100 years [1], involves coating droplets of one phase with small colloidal particles to impede droplet coalescence [2]. The colloidal “armor plating” of these Pickering emulsions also plays a role in colloidosomes, colloid-coated lipid bilayer vesicles used for encapsulation and delivery of flavors, fragrances and drugs [3]. Identical micron-sized particles tend to crystallize under typical experimental conditions, and it is of some interest to understand the defect structure of locally crystalline ground states on a sphere, since these influence the strength of the colloidal armor. Understanding particle packings on a sphere also involves fundamental questions of theoretical physics and mathematics, dating back to work by J. J. Thomson in 1904 [4]. Although Thomson was interested in electrons interacting with a repulsive  $1/r$  potential [5, 6, 7, 8], the problem of determining crystalline ground states on a sphere can be posed more generally in terms of continuum elastic theory, Young’s moduli and defect core energies, for particles interacting with a wide variety of pair potentials [9, 10, 11].

Defects play an essential role in describing crystalline particle packings on the sphere. At least twelve particles with 5-fold coordination (i.e., 12 disclinations) are required for topological reasons, and like the 5-fold rings in carbon fullerenes, one might expect that the energy would be minimized if the disclination positions approximated the vertices of a regular icosahedron. This expectation, which also plays a role in geodesic domes and in the protein capsomere configurations of spherical virus shells [12, 13], is nevertheless *violated* when the shells are sufficiently large and disclination buckling [14] out of the spherical environment is suppressed by surface tension. Consistent with theoretical expectations [7, 8, 9], experiments on particle-coated water droplets in oil [15] reveal that the twelve excess disclinations sprout grain boundary “scars” for sufficiently large  $R/a$ , where  $R$  is the sphere radius and  $a$  is the average particle spacing. When triangulations of microscopic particle packings are used to reveal the local coordination number, these grain boundaries appear as additional dislocations, i.e., 5-7 pairs, arrayed around an unpaired 5, in a pattern such as 5-7-5-7-5-7-5-7-5. Although the critical value of  $R/a$  above which grain boundaries appear depends on microscopic details, both theoretical estimates [9] and experiments [15] indicate that this instability arises as soon as  $R/a \gtrsim 5 - 6$ , i.e., when the total

number of particles exceeds several hundred. Thus, unlike crystals in flat space, dislocations arrayed in grain boundaries are an intrinsic part of the ground state. These grain boundaries can, moreover, stop and start freely on the sphere, unlike their flat space counterparts. Such terminations occur naturally (and with low energy cost) because crystalline grains rotate under parallel transport due to the nonzero Gaussian curvature of the sphere.

If disclinations and dislocations are crucial for understanding spherical crystallography, what can we say about *vacancies and interstitials*, which are well known to play a key role in conventional crystals [16]? It is natural to introduce vacancies and interstitials in an attempt to understand spherical particle packings that deviate from certain “magic numbers”  $N_{nm}$ . These preferred particle numbers, introduced by Caspar and Klug in their analysis of viral shells [12], refer to special commensurate spherical tessellations, indexed by a pair of integers  $(n, m)$ . The corresponding particle number associated with these commensurate particle packings is  $N_{nm} = 10(n^2 + m^2 + nm) + 2$ . It is tempting to ignore the instability to grain boundary scars for large  $N_{nm}$  and regard the commensurate  $(n, m)$  lattice as an interesting metastable state. It would then be natural to introduce vacancies and interstitials to describe candidate ground state packings for  $N_{nm} \pm t$  particles, where  $t = 1, 2, \dots$  and much less than the distance to the next magic number. There is, however, another surprise in store: In contrast to flat space, where vacancy and interstitial defects are stable and well defined, we find that interstitials and vacancies are typically ripped apart into dislocation fragments by the strain fields of nearby 5-fold disclinations. The dislocations then combine with some of the excess 5’s to form defect clusters such 7-5-7. Thus, vacancies and interstitials lose their integrity via fragmentation in spherical crystals, and mediate formation of small grain boundary scars. A full account of the ground states on the sphere for  $N_{nm} \pm t$  particles is beyond the scope of this paper. We present here, however, a study of the fragmentation process itself. We concentrate on interstitials for simplicity. Although vacancies behave in a similar fashion and can be studied by the same computer program [17], the theoretical analysis is more complicated for vacancies, which are typically crushed by elastic forces into objects with a low two-fold symmetry, even in flat space [18, 19]. In addition, we compare our results for interstitial energies (which are position-dependent) to predictions of continuum elastic theory and provide information about the energetics in the vicinity of  $(n, m)$  commensurate spherical tessellations.

We begin by studying in Section 2 the fractionalization of interstitials in two-dimensional curved crystals via numerical simulations of the generalized Thomson problem [17]. Interstitials (or vacancies) in a sufficiently large

spherical crystal are, unlike in flat space, unstable to unbinding into several individual dislocations, each of which glides towards the nearest disclination, eventually forming the small grain boundary scars mentioned above [20]. In this section, we investigate such unstable interstitials and their fractionalization in some detail. We determine the energy of interstitials before and after fragmentation as a function of their position relative to the twelve excess disclinations that are inevitably present in a spherical crystal in Sections 3 and 4. In Section 5, we calculate the interaction energy of interstitials with the extra disclinations within continuum elasticity theory. Finally, we discuss ground state energies close to preferred “magic numbers” of particles on the sphere corresponding to the regular icosahedra of Caspar and Klug [12].

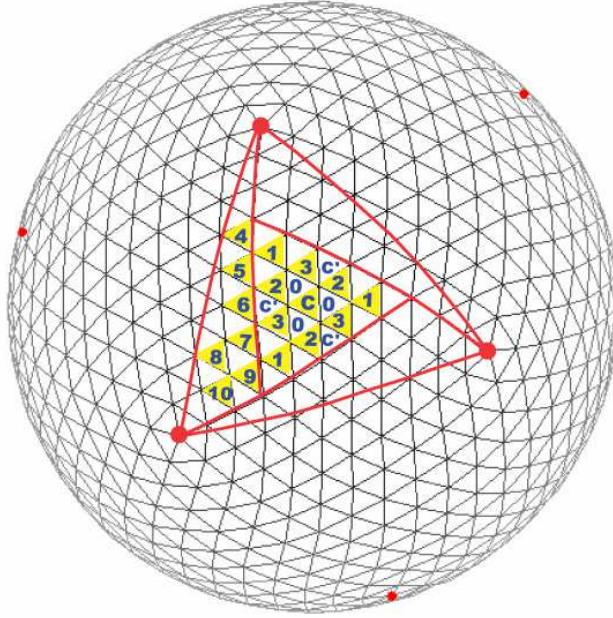


Figure 1: Initial icosahedral configuration of an (8,3) spherical crystal lattice with 12 disclination defects. This lattice is chiral, and is arranged such that 8 steps along a Bragg row, followed by 3 steps to the right along a Bragg row at a  $120^\circ$  angle, connect neighboring 5-fold disclinations. Distinct initial locations for interstitials are shown as triangular plaquettes labeled by characters and numbers.

## 2 Interstitial fractionalization

An icosahedral spherical crystalline lattice (a regular icosadeltahedron) can be constructed for every pair of integers  $(n, m)$ , where the number of vertices or particles in the tessellation is given by the “magic numbers”  $N_{nm}$ :

$$N_{nm} = 10(n^2 + nm + m^2) + 2 . \quad (1)$$

We are interested in studying the effect of inserting an interstitial or a vacancy into a regular  $(n, m)$  icosahedral lattice by adding or removing a single particle, giving rise to particle numbers  $N_{nm} \pm 1$  not falling in the classification of Eq. (1) and in studying the relation of interstitials to the extra dislocation defects (scars) found in spherical crystals above a critical system size [9, 15]. Refs. [18, 19, 21, 22, 23, 24] study configurations and energies of interstitial and vacancy defects and their energetics in triangular lattices in flat space.

The presence of excess dislocation defects in the ground state of spherical crystals is dramatically illustrated by the following numerical experiment: we start with a regular icosadeltahedral tessellation of the sphere – say an  $(8, 3)$ , corresponding to  $N_{83} = 972$  (Fig. 1). This may be done with the applet located at [17] using the Construct  $(m, n)$  algorithm. Although the true ground state for 972 particles on the sphere with most pair potentials has additional dislocation defects (i.e. tightly bound pairs of 5- and 7- coordinated particles) arrayed in grain boundary scars [9], the regular icosadeltahedral lattice is a local minimum from which it is difficult to escape without the addition of thermal noise. In fact it is a major challenge to find fast and reliable algorithms to locate the true ground state (global minimum) in this problem with its complex energy landscape. Now add a single particle to the lattice at the center of mass of a spherical triangle whose vertices are 3 nearest-neighbor 5-fold disclinations (shift + click). The *self-interstitial* so formed is then relaxed by a standard relaxation algorithm, with sufficient thermal noise to allow dislocation glide over the Peierls potential [25]. One immediately finds that an interstitial is structurally unstable. In a few time steps it morphs into a complex of dislocations with zero net Burgers vector. The most common structure observed is a set of three dislocations, with Burgers vectors perpendicular to a line joining each 5-7 pair, inclined at  $120^\circ$  angles to each other. Eventually the interstitial complex is ripped apart entirely, as illustrated schematically in Fig. 2 (see also Fig. 3). Intermediate configurations and final states as the dislocations glide apart will be classified later. Most often three separate dislocations are formed which each glide toward a 5-fold disclination. The end result is the formation of a

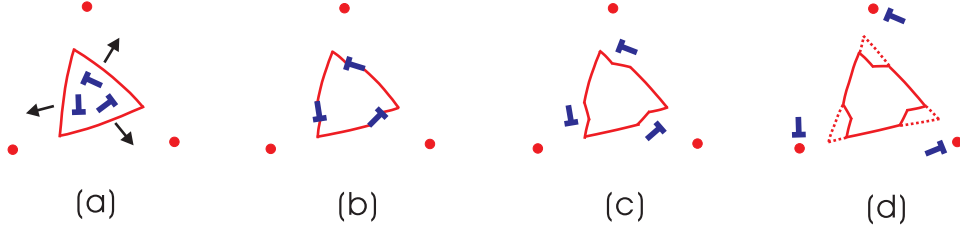


Figure 2: A schematic of interstitial fractionization. The  $\dashv$  symbols are alternative ways of representing dislocations depicted elsewhere as 5-7 pairs.

“mini-scar” (a 5–7–5 grain boundary) at each of the vertex 5s. Subsequent removal of a particle to restore the particle number to the original 972 and relaxing still leaves scars with total energy lower than the starting configuration with 12 isolated 5’s. This observation confirms that scars are definitely lower energy states and not simply artifacts of the relaxation algorithm.

The above phenomenon of low-temperature ( $T \gtrsim 0$ ) *unbinding* of dislocations by spatial curvature is a curved space analog of melting at finite temperature. The extended nature of fractionated interstitials (each separating dislocation component involves an extra row of particles) means that they cannot be treated as small perturbations from the initial spherical crystal with particle number  $N_{nm}$ .

Let’s return to the specific case of the  $N = 973$  particle configuration generated by an interstitial inserted into one triangular plaquette of a regular  $(8, 3)$  lattice of  $N_{nm} = 972$  particles with the requisite 12 disclination defects (5-fold coordinated particles) at the vertices of a regular icosahedron, as shown in Fig. 1. The spherical crystal is distorted by the additional particle – the local configuration adopted by the interstitial changes as the crystal relaxes toward a lower energy state. As in the case of planar lattices, we also find here that the various interstitial defect configurations appear, such as the twofold symmetric interstitial  $I_2$ , the threefold symmetric interstitial  $I_3$ , and the fourfold symmetric interstitial  $I_4$  (see Figs. 3, 4, and 5). The most common intermediate complex formed by the interstitial is threefold symmetric in the rough form of a triangular loop composed of three dislocations with radially oriented Burgers vectors. All of the configurations adopted by an interstitial prior to unbinding can be described as a set of dislocations with zero net Burgers vector.

In marked contrast to interstitial defects in a planar crystal, interstitial defect configurations in a spherical crystal are metastable states with characteristic decay processes. As we shall see, the instability is caused by interac-

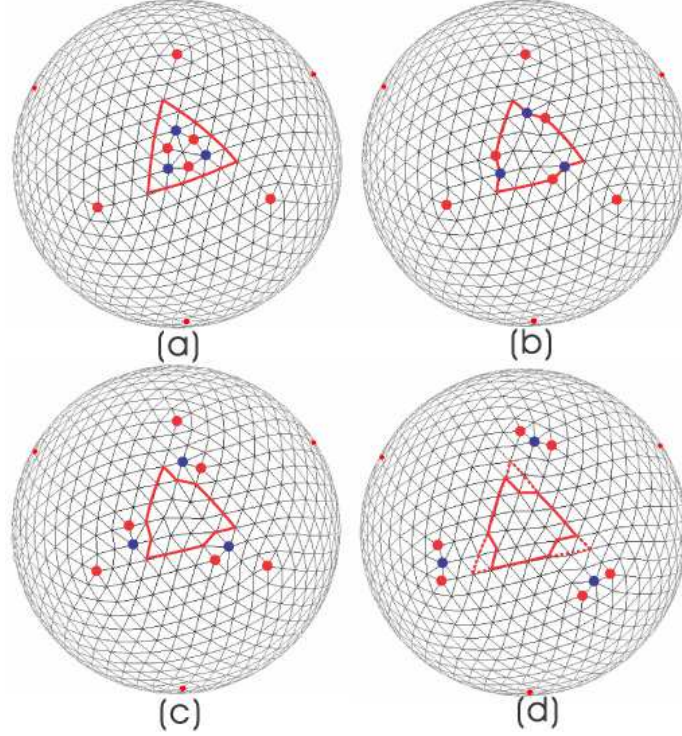


Figure 3: The fractionalization of an interstitial defect inserted at the center of three neighboring disclinations in an  $(8,3)$  spherical tessellation: (a) the initial interstitial defect configuration ( $I_3$ ) shown surrounded by a triangular reference contour; (b) the bound defect unbinds to form three separate dislocations (5-7)- pairs; (c) each dislocation glides (i.e., moves parallel to its Burgers vector) towards the nearest disclination; (d) three mini-grain boundary scars are formed. We also keep track of the evolution of the initial defect in (a) by illustrating the deformation of the triangular contour around the initial defect for (b), (c), and (d) induced by the passage of the dislocation.

tions with the inevitable disclinations associated with the nonzero Gaussian curvature of the sphere. A representative evolution of an interstitial inserted at the center of three neighboring disclinations in an  $(8,3)$  icosadeltahedron is shown in Fig. 3. After some local relaxation the interstitial configuration denoted  $I_3$  is formed, as shown in Fig. 3 (a). We also show there the construction of a triangular contour surrounding the original interstitial defect. The presence of an interstitial follows because the contour encloses 7 par-

ticles instead of 6, the number appropriate to a perfect triangular lattice. During the annealed relaxation illustrated in Figs. 3(b) through (d), the dislocations which are bound together in the initial interstitial unbind into individual dislocations and subsequently glide towards nearby disclinations, eventually forming minimal 5-7-5 grain boundary scars. If one thinks of the initial dislocations as internal degrees of freedom within the interstitial, one could say that one-third of an interstitial is present in each mini-scar in the final state and thus that the interstitial demonstrates  $1/3$  fractionalization. For other initial conditions the fractionation is into two dislocations, each representing  $1/2$  of the original interstitial. The instability of interstitial defects in curved crystals may be studied via continuum elasticity theory by calculating the interaction energies between defects at each stage of the relaxation process of Fig. 3 [20]. We note that the triangular plaquette around the initial defect has been deformed such that it conforms as closely as possible to the regular triangular lattice during the relaxation process. Its deformation reveals the passage of the escaping dislocations.

### 3 Interstitial defect energies

In this section, we discuss the energy of an interstitial defect in a spherical crystal. Consider  $N$  point particles constrained to lie on the two-dimensional surface of a unit sphere. The energy of  $N$  particles interacting through a generalized Coulomb potential within the curved surface is given by

$$E = \frac{1}{2} \sum_{i,j} \frac{1}{|\mathbf{r}_i - \mathbf{r}_j|^s} , \quad (2)$$

where  $\mathbf{r}_i$  is the position of the particle in three dimensions and  $s$  is an integer. For a flat triangular lattice with periodic boundary conditions, the interstitial defect energy at constant density was defined in [21, 22] as

$$E_I = E_{relaxed} - E_{per} , \quad (3)$$

where  $E_{relaxed}$  is the relaxed energy of the rearranged lattice of  $N$  particles with the interstitial defect in the area  $A$ , and  $E_{per}$  is the energy of the perfect crystal at the same areal density  $N/A$ . In curved space, however, the definition of a “perfect crystal” is more subtle, since disclination defects resulting from the Gaussian curvature and the topology are inevitable. We will take as a reference crystal the  $(n, m)$  icosadeltahedral configurations corresponding to triangular tessellations of a magic number of particles



$N_{nm} = 10(n^2 + m^2 + nm) + 2$ . Once an interstitial or vacancy is added to such a  $(n, m)$  configuration, we are no longer at a magic number of particles since these are quite sparsely distributed. We thus need to define the energy of the perfect crystal.

Here we define the energy of the interstitial (vacancy) defect at constant density in the spherical crystal as

$$E_I = E_{local} - E_{annealed}^* , \quad (4)$$

where  $E_{local}$  measures the energy of the relaxed interstitial while the constituent dislocations are still bound and  $E_{annealed}^*$  is the minimum energy of all possible final states attained after *annealed relaxation* leading to interstitial *fractionalization*. This definition will be more explicitly discussed in the following section (see Table 2). We note that both  $E_{local}$  and  $E_{annealed}^*$  are measured at the same areal density  $(N_{nm} \pm 1)/A$ , where  $\pm 1$  correspond to an interstitial (vacancy) respectively. The lowest relaxed energy  $E_{annealed}^*$  plays the role of the energy of the perfect lattice in the planar case at the density of  $(N_{nm} \pm 1)/A$ .

We have performed numerical measurements of  $E_{local}$  and  $E_{annealed}^*$  for the power-law potentials with  $s = 1, 3, 6$  and  $12$ , by adding one interstitial at the center of a spherical triangle formed by three nearest-neighbor disclinations in the  $(8, 3)$  lattice (the location represented by  $C$  in Fig. 1).  $E_{local}$  is measured by quenching the system at the moment just prior to the fractionation of the interstitial into individual dislocations ((a) in Fig. 3). The results are reported in Table 1.

s	1	3	6	12
local	456601.99	2840600.7	$9.62182 \times 10^8$	$3.03015 \times 10^{14}$
annealed	456600.91	2840025.5	$9.60570 \times 10^8$	$3.00313 \times 10^{14}$
$E_{local} - E_{annealed}^*$	1.08	575.2	$0.01612 \times 10^8$	$0.02702 \times 10^{14}$

Table 1: The lowest local and annealed relaxed energy with the central interstitials created by putting a particle at  $C$  in Fig. 1 of the  $(8, 3)$  lattice, for  $s = 1, 3, 6$ , and  $12$ . The differences between two relaxed energies are calculated. Because the particles are embedded in a sphere of unit radius with our conventions, near-neighbor particle spacings are of order  $a \sim N^{-1/2} \ll 1$ , leading to a strong  $s$  dependence in the total energy given by Eq. (2).

## 4 Position dependence of interstitial defect energies

By adding a particle in different plaquettes within the large spherical triangle of Fig. 1, one can explore the dependence of the final state on the initial interstitial location. In contrast to the case for planar crystals, both the *location* and *orientation* of the interstitial defect relative to nearby disclinations influences the resultant configuration and its corresponding evolution, leading to distinct relaxed configurations.

The insertion of a particle at the center of the large spherical triangle leads to an  $I_3$ -type initial configuration, whereas adding the interstitial to the plaquette along an edge results in an  $I_2$ -type initial configuration.

During the relaxation process, we also find that the dislocation complex representing an interstitial can rotate so as to reorient the Burgers vectors so that constituent dislocations can glide towards a nearby disclination and bind to it. This phenomenon is especially noticeable if we place one extra particle slightly off from the absolute center  $C$ , such as the locations  $C'$  or 0 in Fig. 1.

In Fig. 4 and Fig. 5 we illustrate this phenomenon more explicitly. In Fig. 4(a), an interstitial initially placed at the position  $C'$  in Fig. 1 morphs quickly to an  $I_3$  configuration. In (a), however, the orientations of the dislocations within  $I_3$  are not appropriate for dislocation glide to the surrounding disclinations since the 5 end of the dislocations point towards rather than away from these 5-fold disclinations, causing them to be repelled. Glide-induced fractionalization is therefore prohibited in this orientation. Re-

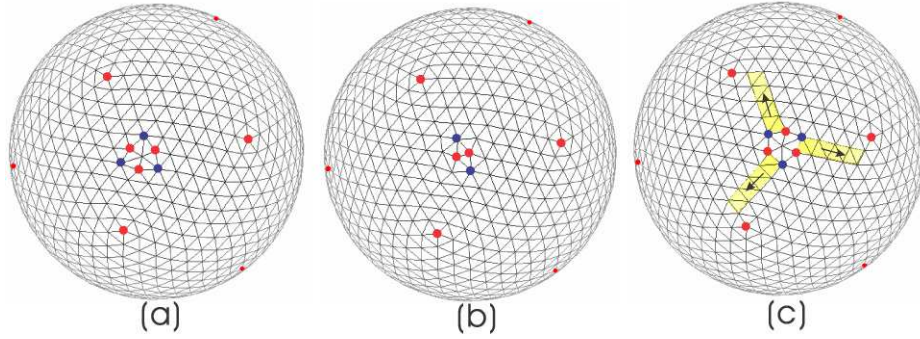


Figure 4: The rotational motion of an interstitial configuration (created with the initial location  $C'$  in Fig. 1) mediated by the transition:  $I_3 \rightarrow I_2 \rightarrow I_3$

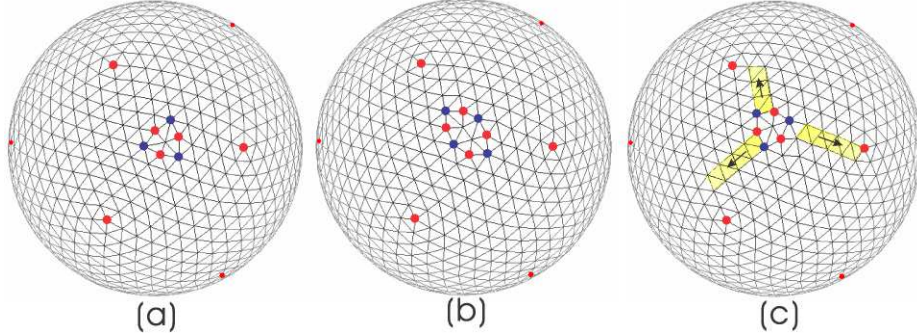


Figure 5: The rotational motion of an interstitial configuration (created with the initial location 0 in Fig. 1) mediated by the transition:  $I_3 \rightarrow I_4 \rightarrow I_3$

markably, though, the entire complex of dislocations can change its orientation by a transition through an intermediate  $I_2$  configuration (shown in Fig. 4(b)) and subsequently to a second  $I_3$  configuration (Fig. 4(c)). The final  $I_3$  configuration is rotated by  $60^\circ$  with respect to the first  $I_3$  and can now fractionate analogously to an interstitial with initial position  $C$  in Fig. 1.

We also find rotational reorientation of an interstitial defect with an  $I_4$ -type intermediate state, as shown in Fig. 5. This particular relaxation process reveals an interesting feature of dislocation dynamics on a curved surface. The  $I_3$  configuration generated after the intermediate (see Fig. 5(c)) now has one dislocation with its glide plane such that it can glide head-on into a vertex disclination. This disclination absorbs the dislocation but hops over one lattice spacing to accommodate the curved space Burgers vector. The other two dislocations end up bound in the form of mini-scars. In this case then the interstitial has fractionated into 2 rather than 3 parts and one say that there has been  $1/2$  fractionization of the interstitial. Absorption and emission of dislocations by 5-fold disclinations are somewhat analogous to absorption and emission of vacancies and interstitials by dislocations (allowing dislocations to climb), a phenomenon well-known in flat space.

We next catalog the dependence of the final state on the initial location of the interstitial. The distinct initial conditions shown in Fig. 1 lead to three different final annealed states, as summarized in Table 2. We have checked that all other possible initial conditions, not indexed in Fig. 1, also produce one of the listed final states. The final state with three mini-scars of the form 5-7-5 has the lowest energy of all final states and provides a measure of  $E_{annealed}^*$ .

It is also informative to track the position dependence of the interstitial

initial location	$E_{annealed}$	annealed state
C, C', 7, 8, 10	$9.60570 \times 10^8$	3 scars (5-7-5)
0, 2, 3, 4, 6, 9	$9.61011 \times 10^8$	2 scars (5-7-5)
1, 5	$9.61062 \times 10^8$	2 scars (5-7-5-7-5)

Table 2: The three classes of final annealed state depending on the initial interstitial location. The relaxed energies are measured for the power law potential  $s = 6$ . Here  $E_{annealed}$  with 3 scars corresponds to  $E_{annealed}^*$ .

energy after it relaxes. Numerical measurements of local relaxed energy for the interstitial as a function of initial location are presented in Table 3. We note that, in most cases, the initial  $I_3$  complexion undergoes transitions to more stable interstitial configurations, except the configuration that starts from the very center location  $C$  in Fig. 1. For the initial conditions,  $C$ ,  $C'$ , 0, and 3,  $I_3$  is the most stable. We also note that the interstitial created at the exact center  $C$  has the lowest defect energy, while one nearest to the disclination from the location 10 requires the largest energy for interstitial defect formation.

n	transition	$E_{local}$ of $I_3$	$E_{local} - E_{annealed}^*$
C	$I_3$	$9.62182 \times 10^8$	$0.01612 \times 10^8$
C'	$I_3 \rightarrow I_2 \rightarrow I_3$	$9.62195 \times 10^8$	$0.01655 \times 10^8$
0	$I_3 \rightarrow I_4 \rightarrow I_3$	$9.62274 \times 10^8$	$0.01708 \times 10^8$
1	$I_3 \rightarrow I_2$	$9.62391 \times 10^8$	$0.01820 \times 10^8$
2	$I_3 \rightarrow I_2$	$9.62296 \times 10^8$	$0.01725 \times 10^8$
3	$I_3$	$9.62269 \times 10^8$	$0.01698 \times 10^8$
4	$I_3 \rightarrow I_2$	$9.62595 \times 10^8$	$0.02025 \times 10^8$
5	$I_3 \rightarrow I_2$	$9.62479 \times 10^8$	$0.01909 \times 10^8$
6	$I_3 \rightarrow I_2$	$9.62420 \times 10^8$	$0.01849 \times 10^8$
7	$I_3 \rightarrow I_2$	$9.62350 \times 10^8$	$0.01780 \times 10^8$
8	$I_3 \rightarrow I_4$	$9.62494 \times 10^8$	$0.01924 \times 10^8$
9	$I_3 \rightarrow I_2$	$9.62526 \times 10^8$	$0.01956 \times 10^8$
10	$I_3 \rightarrow I_4$	$9.62608 \times 10^8$	$0.02037 \times 10^8$

Table 3: The energy of interstitial defects created at different initial positions within the spherical crystal. The energies shown are for a power law potential with  $s = 6$

## 5 Continuum elastic theory calculations

In this section we study interstitials analytically using continuum elastic theory on the sphere. Depending on where we create interstitials within a spherical crystal, we have seen that they lead to different annealed states. One can also understand such position dependency of interstitial defects by calculating the elastic interaction energy of, for example, the threefold symmetric interstitial  $I_3$  with the embedded 12 disclinations. Here, we model an interstitial by a compact 5-7-5-7-5-7 “ring” structure before the fractionization of the bound dislocations into three isolated 5-7 dislocations. If  $\mathbf{x}$  represents a coordinate system within the sphere, the stress field associated with such configuration is determined by the bi-harmonic equation of a sphere in terms of the Airy stress function  $\chi(\mathbf{x})$ , whose sources are the defect density of disclinations  $S_D(\mathbf{x})$ , the defect density of interstitials  $S_I(\mathbf{x})$ , and the Gaussian curvature  $K(\mathbf{x})$  of the background crystal,

$$\frac{1}{Y}\Delta^2\chi(\mathbf{x}) = S_D(\mathbf{x}) + S_I(\mathbf{x}) - K(\mathbf{x}) , \quad (5)$$

where  $Y$  is the two-dimensional Young’s modulus [9]. The defect densities of disclinations and interstitials on a curved crystalline background are, respectively, written as

$$S_D(\mathbf{x}) = \frac{\pi}{3\sqrt{g(\mathbf{x})}} \sum_{\alpha=1}^N q_{\alpha} \delta(\mathbf{x} - \mathbf{x}_{\alpha}) , \quad (6)$$

and

$$S_I(\mathbf{x}) = \frac{1}{2\sqrt{g(\mathbf{x})}} \sum_{\beta=1}^N \Omega_{\beta} \Delta \delta(\mathbf{x} - \mathbf{x}_{\beta}) , \quad (7)$$

where  $g(\mathbf{x})$  is the determinant of the metric tensor of the sphere,  $q_{\alpha}$  is the disclination charge, and  $\Omega_{\beta}$  is the local area change caused by adding an interstitial [26]. For 5- and 7-fold disclinations, we have  $q_{\alpha} = +1$  and  $q_{\alpha} = -1$ , respectively. The elastic free energy in terms of  $\chi(\mathbf{x})$  is given by

$$F = \frac{1}{Y} \int dA (\Delta\chi(\mathbf{x}))^2 , \quad (8)$$

with the area element  $dA = d^2\mathbf{x}\sqrt{g(\mathbf{x})}$ . The interaction energy for a distribution of two different kinds of defects located at positions  $\{\mathbf{x}_{\alpha}\}$  and  $\{\mathbf{x}_{\beta}\}$ , is then obtained from [9]

$$\mathcal{U}(\mathbf{x}_{\alpha}, \mathbf{x}_{\beta}) = Y \int dA_{\mathbf{x}} S_D(\mathbf{x}) \int dA_{\mathbf{y}} \frac{1}{\Delta_{\mathbf{xy}}^2} S_I(\mathbf{y}) . \quad (9)$$

By substituting Eqs. (6) and (7) into Eq. (10) and integrating by parts, the resulting elastic interaction of interstitials at position  $(\theta_\beta, \phi_\beta)$ , with disclinations at position  $(\theta_\alpha, \phi_\alpha)$  lying in the spherical crystalline background, then reduces to

$$\mathcal{U}(\theta_\alpha, \phi_\alpha; \theta_\beta, \phi_\beta) = \frac{Y\pi}{6} \sum_{\alpha, \beta} q_\alpha \Omega_\beta \Delta\chi(\theta_\alpha, \phi_\alpha; \theta_\beta, \phi_\beta) . \quad (10)$$

Here, the interstitial-disclination interaction potential is given by

$$\Delta\chi(\gamma) = \frac{1}{4\pi} \left[ -\ln \left( \frac{1 - \cos \gamma}{2} \right) - 1 \right] , \quad (11)$$

with the angular geodesic distance,  $\gamma$ , between points  $(\theta_\alpha, \phi_\alpha)$  and  $(\theta_\beta, \phi_\beta)$ , given by

$$\cos \gamma = \cos \theta_\alpha \cos \theta_\beta + \sin \theta_\alpha \sin \theta_\beta \cos(\phi_\alpha - \phi_\beta) . \quad (12)$$

We note that this interaction depends logarithmically on distance for small  $\gamma$ , and corresponds to a repulsive interaction when both  $q_\alpha$  and  $\Omega_\beta$  are positive, as is the case for a 5-fold disclination interacting with an interstitial. We expect that similar results hold in flat space.

To understand the results for a spherical geometry in more detail, we first plot the contribution to the elastic potential energy Eq. (10) of a single interstitial as well as a single vacancy versus the angular distance  $\gamma$  to a single 5-fold disclination with the topological charge  $q = +1$  (see Fig 6). We assume that the magnitudes of the area change  $\Omega$  are the same for both defects. The sign of  $\Omega$  can be determined by comparison with the numerical results.  $\Omega > 0$  corresponds to the interstitial, while  $\Omega < 0$  to the vacancy [26]. The calculation indicates that the elastic deformation energy associated with the nucleation of an interstitial falls off with the angular distance from the disclination, whereas the elastic interaction of a vacancy grows with distance. Thus interstitials are repelled by a 5-fold disclination (similar to the discussion of the small  $\gamma$  limit above), whereas vacancies are attracted. Conversely, our calculations suggest that interstitials are attracted to the cores of 7-fold disclinations while vacancies are repelled. This is of interest in constructing ground states on negatively-curved (hyperbolic) spaces. As noted, however, interstitials or vacancies typically break up when subjected to interactions with multiple disclinations.

We now calculate the energy of an interstitial interacting with all twelve disclinations of the spherical crystal in order to compare this continuum prediction to our numerical results. We first create interstitials at various locations with snapshots displayed in Fig. 7. Note that the configurations whose

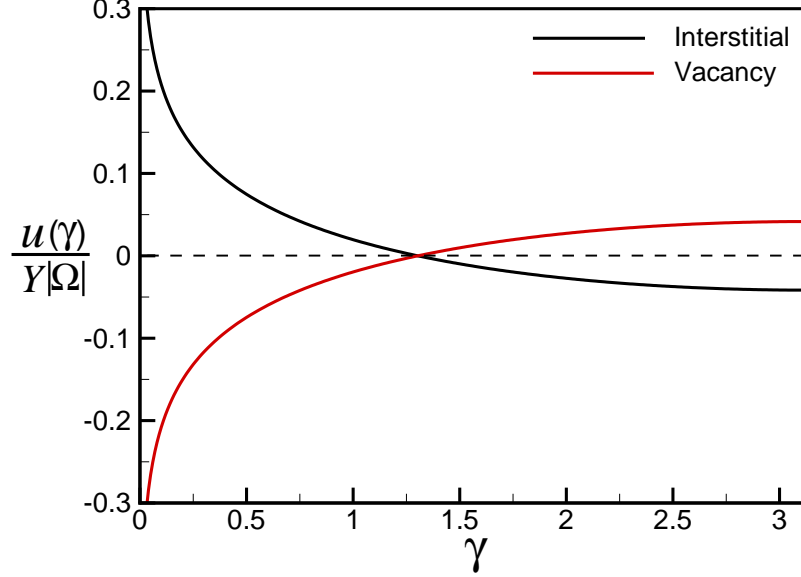


Figure 6: The elastic interaction energies of an interstitial and a vacancy with a single disclination,  $\mathcal{U}(\gamma)$ , are plotted in the unit of  $Y|\Omega|$ .

energies are measured arise from distinct creations of interstitials rather than from snapshots of the evolution of a single interstitial. In Fig. 7(a) we show the configuration resulting from adding a particle at the very center of the spherical triangle (initial position  $C$ ). The effect of shifting the location of the nucleated interstitial off the center towards the isolated disclination at the bottom left is shown in Figs. 7(b) through (e). Finally Fig. 7(f) illustrates the case of creation immediately adjacent to the disclination. For each nucleation of an interstitial we obtain the relaxed energy  $E_{local}$  after *local relaxation* immediately prior to unbinding into individual dislocations (fractionization). The numerical results are scaled (this amounts to taking the product of the Young's modulus  $Y$  and the extra area  $\Omega$  of the interstitial as a fitting parameter) to compare with the analytic calculation discussed below and presented, with error bars, in Fig. 8.

For each configuration in Fig. 7, the continuum elastic potential ener-

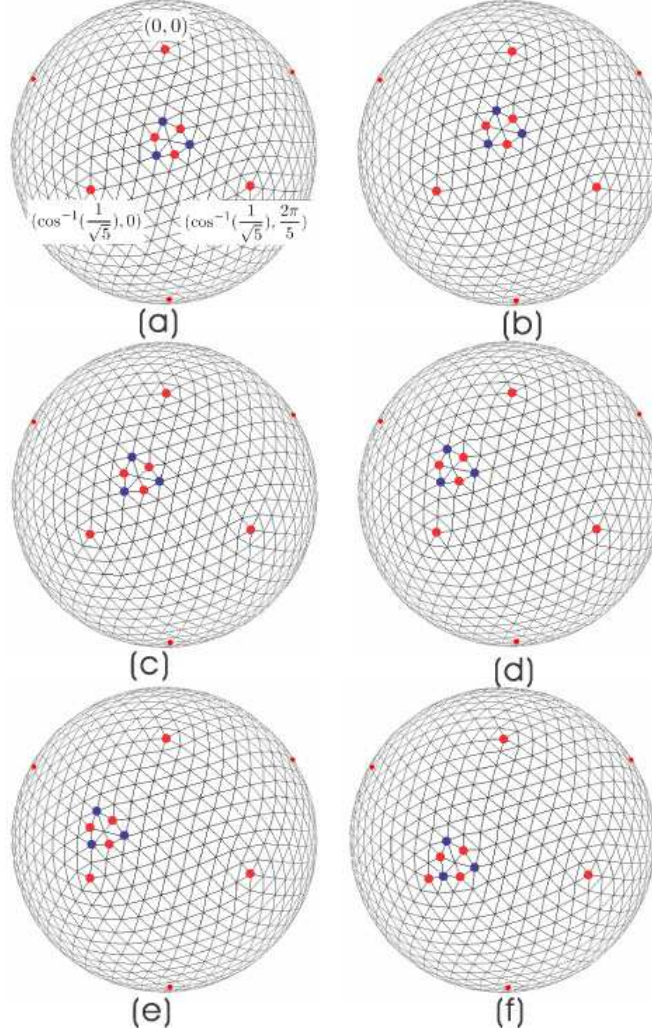


Figure 7: Snapshots of interstitials created at various locations relative to neighboring disclinations. As indicated in part (a), the disclination at the top vertex is located at the north pole,  $(0,0)$ , while those at the bottom left and right are at polar angles  $(\cos^{-1}(1/\sqrt{5}), 0)$  and  $(\cos^{-1}(1/\sqrt{5}), 2\pi/5)$ , respectively. The locations of the center of each interstitial,  $(\theta_I, \phi_I)$ , are approximately estimated using spherical trigonometry: (a)  $(0.65, \pi/5)$  (b)  $(0.60, 0.54)$  (c)  $(0.63, 0.33)$  (d)  $(0.65, 0)$  (e)  $(0.77, 0)$  (f)  $(0.97, 0.21)$ , where all angles are in radians.



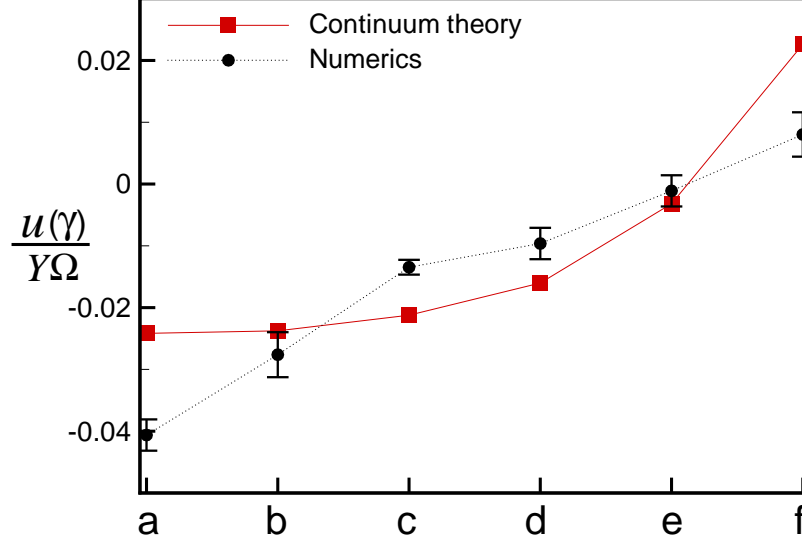


Figure 8: For the selected locations of interstitials within the  $(8, 3)$  lattice in Fig. 7, the elastic interaction energy of an interstitial with all twelve disclinations is plotted in the units of  $Y\Omega$ , with interstitial locations  $a - f$  arranged in order of increasing  $\gamma$ . The circles with error bars represent numerically measured results which are re-scaled to fit the analytic calculations.

gies including all 12 disclinations can be obtained by inserting the known spherical coordinates of the disclinations. For the twelve vertices of the icosahedron, we choose the following explicit coordinates,

$$(\theta, \phi) \equiv \left\{ (0, 0), \left( \delta, \frac{2\pi k}{5} \right)_{0 \leq k \leq 4}, \left( \pi - \delta, \frac{\pi}{5} + \frac{2\pi k}{5} \right)_{0 \leq k \leq 4}, (\pi, 0) \right\}, \quad (13)$$

where  $\delta = \cos^{-1}(1/\sqrt{5}) \approx 1.107$  radian. The first 6 vertices lie in the northern hemisphere and the remaining 6 in the southern hemisphere. The location of the center of the interstitial is estimated by a simple counting of lattice spacings together with spherical trigonometry:  $\cos c = \cos a \cos b +$

$\sin a \sin b \cos C$ , where  $a$ ,  $b$ , and  $c$  are the angular lengths of the sides of the spherical triangle, and  $C$  is the angle of the triangle that faces the side  $c$ . The coordinates so obtained are given in the caption of Fig. 7. The resulting total elastic coupling energies of the interstitials with all disclinations, corresponding to the configurations in Fig. 7, are plotted together with the numerical results in Fig. 8. As can be seen, there is reasonable agreement between our numerical results and continuum elastic theory on the sphere.

## 6 Vicinity of the magic number

Icosadeltahedral configurations of magic numbers  $N_{nm}$  of particles on the sphere are believed to be good approximations to ground states for relatively small numbers of particles, say  $N \lesssim 300$ , interacting via a Coulomb potential [27]. In this section we investigate the role of interstitials and vacancies on the energetics of  $N$  particles in the vicinity of the magic numbers  $N_{nm}$ .

The energy of the system of particles interacting with a power-law potential Eq. (2) can be expressed as an expansion in powers of the total number of particles  $N$ , for  $0 < s < 2$ ,

$$2E_{TOT}(N) = \left[ \frac{N^2}{2^{s-1}(2-s)} - a_1 N^{1+\frac{s}{2}} + \mathcal{O}(N^{s/2}) \right] \frac{e^2}{R^s}, \quad (14)$$

where the coefficient  $a_1$  is a term determined by the geometry and the microscopic potential [10, 11]. We will choose units such that  $e^2/R^s$  is unity for our purposes here. For  $s > 2$ , the first term in Eq. (14), which arises from long-range interactions, is missing. The coefficient  $a_1$  may be obtained by calculating the correction to the zero mode energy associated with a particular defect configuration via the continuum elastic model [11], or by fitting the energy from exact minimizations with the function Eq. (14) [28].

To study the total energy in the vicinity of the magic number  $N_{nm}$ , it is useful to compare the relaxed energies of particle numbers  $N = N_{nm} \pm t$  along with the inserted interstitial or vacancy defects  $t$ , to the expression Eq. (14) in terms of  $N$ . For this comparison, we use

$$E_{fitted} = \frac{1}{2}(N^2 - 1.10494N^{3/2}), \quad (15)$$

where  $a_1$  was obtained from the icosahedral configuration of twelve 5-fold disclinations with  $s = 1$  [11]. Although this value of  $a_1$  is an approximate continuum result, the value above provides a smoothly varying background energy  $E_{fitted}(N)$  useful for our purposes.

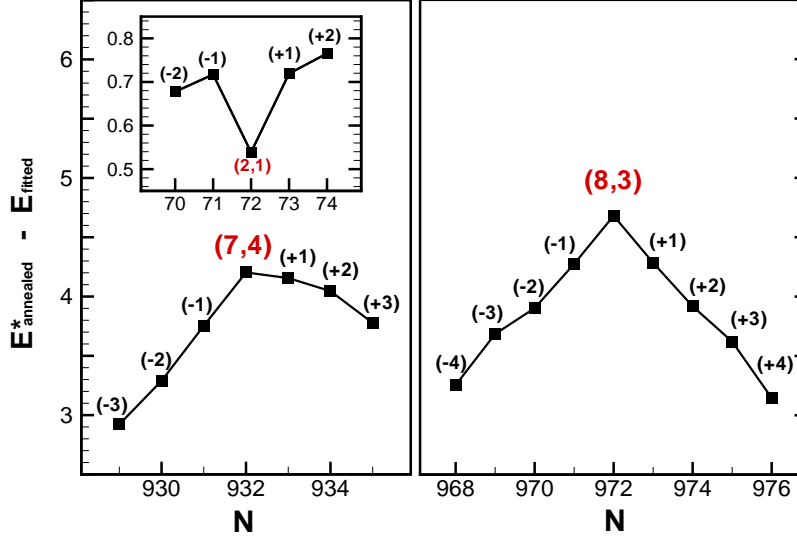


Figure 9: We plot the difference between the numerically fitted energy and the annealed energy with interstitials and vacancies in the vicinity of the icosadeltahedral configurations with magic numbers 932, 972, and 72 (inset) for the case of Coulomb interactions,  $s = 1$ . The total particle numbers are thus  $N_{nm} + t$ , where the integer  $t$  is given in parentheses above each data point. Note that  $E$  is dimensionless in our units for this section.

In Fig. 9, we plot  $E^*_{\text{annealed}} - E_{\text{fitted}}$  in the vicinity of the (8,3) icosadeltahedral lattice with  $N_{83} = 972$ , (7,4) with  $N_{74} = 932$ , and (2,1) with  $N_{21} = 72$ , where  $E^*_{\text{annealed}}$  is the lowest annealed energy we found for incommensurate particle numbers created initially by inserting interstitials or vacancies. For large  $N$ , such as 932 and 972, we find that the icosadeltahedral configuration is a local maximum rather than a local minimum. Inserting interstitials (or vacancies) lowers the energy. Presumably, this lowering of the total energy arises because, as we have shown, vacancies and interstitials facilitate formation of grain boundary scars, favored for  $N \gtrsim 300$ . For relatively small numbers of particles, on the other hand, such as  $N = 72$ , the icosadeltahedral configuration is a local minimum, consistent with expectations for  $N \lesssim 300$  [9]. Somewhat similar results near special numbers of capsids were found in a minimal model for the equilibrium energy of viral

capsids using Monte Carlo simulations [13].

### Acknowledgements

The work of MJB and HS was supported by the NSF through Grants DMR-0219292 and DMR-0305407, and through funds provided by Syracuse University. The work of DRN was supported by the Harvard MRSEC through Grant DMR-0213805.

### References

- [1] S. Pickering, J. Chem. Soc. **91**, 2001 (1907).
- [2] S. Sacanna, W. K. Kegel and A. P. Philipse, Phys. Rev. Lett. **98**, 158301 (2007), and references therein.
- [3] A. D. Dinsmore, M. F. Hsu, M. G. Nikolaides, M. Marquez, A. R. Bausch, and D. A. Weitz, Science **298**, 1006 (2002).
- [4] J. J. Thomson, Philos. Mag. **7**, 237 (1904).
- [5] M. J. W. Dodgson and M. A. Moore, Phys. Rev. B **55**, 3816 (1997).
- [6] A. Perez-Garrido, M. J. W. Dodgson and M. A. Moore, Phys. Rev. B **56**, 3640 (1997).
- [7] A. Toomre, unpublished work
- [8] A. Perez-Garrido and M. A. Moore, Phys. Rev. B **60**, 15628 (1998).
- [9] M. J. Bowick, D. R. Nelson and A. Travesset, Phys. Rev. B **62**, 8738 (2000).
- [10] M. Bowick, A. Cacciuto, D. R. Nelson and A. Travesset, Phys. Rev. Lett. **89**, 185502 (2002).
- [11] M. J. Bowick, A. Cacciuto, D. R. Nelson and A. Travesset, Phys. Rev. B **73**, 024115 (2006).
- [12] D. L. D. Caspar and A. Klug, Cold Spring Harb Symp. Quant Biol. **27**, 1 (1962).
- [13] R. Zandi, D. Reguera, R. F. Bruinsma, W. M. Gelbart and J. Rudnick, Proc. Natl. Acad. Sci. U.S.A. **101**, 15556 (2004).

- [14] J. Lidmar, L. Mirny and D. R. Nelson, Phys. Rev. E **68**, 051910 (2003)
- [15] A. R. Bausch, M. J. Bowick, A. Cacciuto, A. D. Dinsmore, M. F. Hsu, D. R. Nelson, M. G. Nikolaides, A. Travesset and D. A. Weitz, Science **299**, 1716 (2003).
- [16] N. W. Ashcroft and N. David Mermin, *Solid State Physics* (Brooks/Cole Thomson Learning, 1976) Chapter 30.
- [17] M. Bowick, C. Cecka and A. Middleton, <http://physics.syr.edu/condensedmatter/thomson/>.
- [18] E. Cockayne and V. Elser, Phys. Rev. B **43**, 623 (1991)
- [19] S. Jain and D. R. Nelson, Phys. Rev. E **61**, 1599 (2000).
- [20] M. Bowick, H. Shin and A. Travesset, Phys. Rev. E **75**, 021404 (2007).
- [21] D. S. Fisher, B. I. Halperin and R. Morf, Phys. Rev. B **20**, 4692 (1979).
- [22] E. Frey, D. R. Nelson and D. S. Fisher, Phys. Rev. B **49**, 9723 (1994).
- [23] A. Pertsinidis and X.S. Ling, Nature **413**, 147 (2001); Phys. Rev. Lett. **87**, 098303 (2001); New J. Phys. **7**, 33 (2005).
- [24] A. Libal, C. Reichhardt and C.J. Olson Reichhardt, Phys. Rev. E **75**, 011403 (2007).
- [25] P. Lipowsky, M. J. Bowick, J. H. Meinke, D. R. Nelson and A. B. Bausch, Nature Materials **4**, 407 (2005).
- [26] D. R. Nelson, *Defects and Geometry in Condensed Matter Physics* (Cambridge University Press, Cambridge 2002).
- [27] E. L. Altschuler, T. J. Williams, E. R. Ratner, R. Tipton, R. Stong, F. Dowla and F. Wooten, Phys. Rev. Lett. **78**, 2681 (1997).
- [28] E. L. Altschuler and A. Perez-Garrido, Phys. Rev. E **73**, 036108 (2006).